

Multimodal Differential Phase Contrast and Fluorescence Microscopy For Characterizing Protein Aggregation

William Xu



Electrical Engineering and Computer Sciences
University of California, Berkeley

Technical Report No. UCB/EECS-2025-101

<http://www2.eecs.berkeley.edu/Pubs/TechRpts/2025/EECS-2025-101.html>

May 16, 2025

Copyright © 2025, by the author(s).
All rights reserved.

Permission to make digital or hard copies of all or part of this work for personal or classroom use is granted without fee provided that copies are not made or distributed for profit or commercial advantage and that copies bear this notice and the full citation on the first page. To copy otherwise, to republish, to post on servers or to redistribute to lists, requires prior specific permission.

**Multimodal Differential Phase Contrast and Fluorescence Microscopy For
Characterizing Protein Aggregation**

by William Xu

Research Project

Submitted to the Department of Electrical Engineering and Computer Sciences, University of California at Berkeley, in partial satisfaction of the requirements for the degree of **Master of Science, Plan II**.

Approval for the Report and Comprehensive Examination:

Committee:

Laura Waller

Professor Laura Waller
Research Advisor

05/16/2025

Date

* * * * *

Guanghan Meng

Professor Guanghan Meng
Second Reader

05/16/2025

Date

Abstract

This work describes the experimental setup for automated acquisition of cell samples using Differential Phase Contrast (DPC) and Fluorescence microscopy. As opposed to labeled methods which require toxic chemical stains that damage the structure of cells and tissue, our methods are label-free, requiring only hardware modifications to a commercial microscope.

We provide the implementation of automated acquisition of DPC images, both 2D and 3D, in a commercial microscope with an LED array as its illumination source. We conducted real-world experiments in which we gathered a large dataset of spatially registered DPC and fluorescence images of U2OS (human osteosarcoma) cells. The application of these techniques is explored in characterizing toxic protein aggregations in these samples.

Acknowledgements

I would like to thank my advisor Professor Laura Waller for her guidance throughout the course of this Masters' program. I have learned so much about the field of computational imaging from her teaching in EE290F and from listening in on group meetings over the past year. I would also like to thank Professor Guanghan Meng for her mentorship and assistance on various research projects over the past 2 years, and our collaborator Shenjie Wu for providing us the samples used in this work. Finally, I would like to thank my family and friends for supporting my pursuit of this degree.

Table of Contents

1. Related Work
 - a. Quantitative Phase Imaging
 - b. Differential Phase Contrast
 - c. Aberration Correction
 - d. Biological Applications
2. Multimodal Imaging Setup
3. U2OS Cell Dataset
 - a. Segmentation and QPI Reconstruction
 - b. Autofluorescence
4. Statistical Analysis of DPC Measurements
5. Deep Learning for characterizing Protein Aggregation
6. Future Work

Figure/Equation Descriptions

Figures

Figure 1.1. Programmable LED dome array, with several LEDs turned on during “demo mode”

Figure 1.5. Phase, absorption WOTF plots for half-circle illumination

Figure 1.8. QPI reconstructions using Tikhonov regularization exhibiting high frequency noise

Figure 1.9. Example aberration map and its decomposition obtained using the Zernike Basis

Figure 1.10. TV-regularized quantitative phase map

Figure 1.11. Pupil phase for a simulated aberration including a large coefficient for the Defocus aberration mode

Figure 1.12. Aberrated DPC WOTFs simulated using the aberration phase map from Figure 2.11

Figure 1.13. Simulated beads under aberrated vs unaberrated DPC forward models

Figure 2.1. Multimodal imaging setup

Figure 2.2. Excitation and emission spectra for TAMRA

Figure 3.1. DPC intensity images of U2OS cells from dataset, along with their Fourier transforms

Figure 3.2. Coarse segmentation of individual U2OS cells, produced by fine-tuned Cellpose model

Figure 4.1. Ilastik feature selections for input into Random Forest classifier

Figure 4.2. Example Ilastik fine segmentations with post-processing

Figure 4.1. QPI reconstruction of single U2OS cell, with overlay of fluorescence labels

Figure 5.2. Classifier performance on held-out dataset

Figure 6.1. Lateral and axial cross-sections of 3D QPI reconstructions on test object (borosilicate microsphere)

Figure 6.2. 3D rendering of sample 3D refractive index

Figure 6.3. Comparison of Phase WOTFs from annular vs half-circle illumination patterns

Figure 6.4. Comparison of Phase WOTFs from annular vs half-circle illumination patterns

Equations

Equation 1.2. DPC intensity as a function of source and pupil functions using the forward intensity model of a 4-f system

Equation 1.3. DPC intensity under the assumption of Köhler Geometry, approximated as the sum of contributions from point sources

Equation 1.4. Closed-form expressions for DPC WOTFs for phase and absorption

Equation 1.6. DPC deconvolution inverse problem using L2-regularization (Tikhonov)

Equation 1.7. Closed-form solution to DPC deconvolution using L2 regularization

1. Related Work

1a. Quantitative Phase Imaging

Quantitative Phase Imaging (QPI) is a method to produce mappings of the phase delays corresponding to differences between an object's thickness and refractive index from its surroundings. In the 2D case [7, 9, 20], QPI phase maps measure the change in refractive index

integrated along the thickness of the sample. This yields the relation $\phi = \frac{2\pi}{\lambda} \int ndz$. In the 3D case [8], a 3D forward model based on a 3D volume's scattering potential is used. 3D QPI reconstruction methods disentangle thickness from refractive index, allowing for reconstruction of the refractive index.

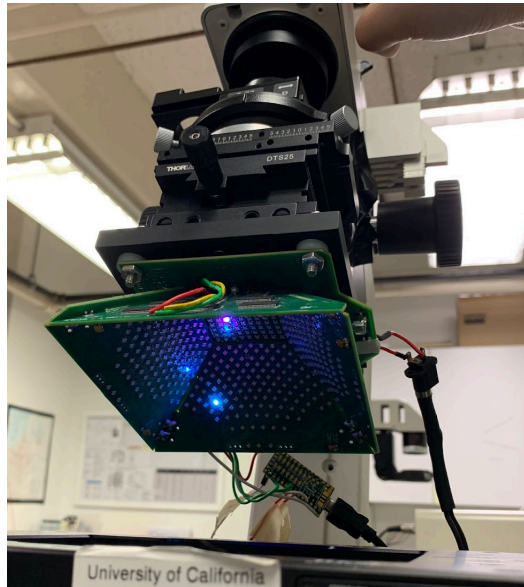


Figure 1.1: Our Programmable LED dome unit replaces the condenser and light source of a commercial microscope. The LED dome allows for control over the intensity, illumination wavelength, and illumination pattern.

In many QPI techniques, multiple intensity images are captured and a reconstruction algorithm is used to estimate phase and amplitude information. Several techniques can be implemented on a programmable LED Array [1], which provides flexible control over illumination angles and wavelengths. One well known QPI technique is Fourier Ptychographic Microscopy (FPM) [9]. Fourier Ptychography uses angled illumination (single-LED) to shift an object's spectrum in Fourier space, and low NA intensity images are taken under many different illumination angles. Each coherent-illumination image samples a small region of the object's spectrum in Fourier Space. An iterative algorithm is used to stitch together these samples in order to reconstruct the object's transmission function. The resulting reconstruction contains an effective NA of

($NA_{\text{objective}} + \max(NA_{\text{illumination}})$), where the second term can be as great as 0.8 using our LED array. Thus Fourier ptychography enables wide-FOV high resolution images.

1b. Differential Phase Contrast

Coherent illumination techniques such as Fourier Ptychography are very sensitive to misalignments in the illumination system, as well as to system aberrations and debris in the optical path. Furthermore, FPM requires heavy compute overhead, and many different measurements due to a large degree of overlap in Fourier space being necessary between single-LED measurements in order for the reconstruction algorithm to properly converge. In contrast to FPM, differential phase contrast (DPC) [7] uses partially coherent illumination. Compared to FPM, DPC provides an imaging modality that is less sensitive to system misalignment and requires far fewer measurements. As opposed to illumination from a coherent source, the usage of partially coherent illumination provides a distinct focus plane. This section contains a detailed discussion of the DPC forward model and phase retrieval methods.

In a typical 4-f system, the intensity at the image plane resulting from coherent illumination from a point source can be derived as follows. Illumination by angled illumination introduces a phase ramp corresponding to illumination angle. At the Fourier plane, the sample's spectrum is thus shifted according to this phase term, and subsequently low-pass filtered by the objective. Equation 2 shows the full form of this forward model. q and o represent the illumination field and the object's complex transmittance function respectively. u'' denotes spatial dimensions in the Fourier Plane, r denotes spatial coordinates in the object plane. P is the pupil function, which is a circular function with radius dependent on NA and illumination wavelength in the unaberrated case.

$$I(\mathbf{r}_c) = \left| \iint \left[\iint q(\mathbf{r})o(\mathbf{r}) \exp(-i2\pi\mathbf{r} \cdot \mathbf{u}'') d^2\mathbf{r} \right] P(\mathbf{u}'') \exp(-i2\pi\mathbf{u}'' \cdot \mathbf{r}_c) d^2\mathbf{u}'' \right|^2$$

Equation 1.2

Under the Köhler geometry, the intensity corresponding to Differential Phase Contrast is derived from integrating over the source pattern, which represents summing over the contributions of single LED's. This is shown in Equation 1.3. The additional variable u' represents coordinates at the source plane, thus summing these contributions.

$$I(\mathbf{r}_c) = \iint \left| \iint \left[\iint q(\mathbf{r})o(\mathbf{r}) \exp(-i2\pi\mathbf{r} \cdot \mathbf{u}'') d^2\mathbf{r} \right] P(\mathbf{u}'') \exp(-i2\pi\mathbf{u}'' \cdot \mathbf{r}_c) d^2\mathbf{u}'' \right|^2 d^2\mathbf{u}'$$

Equation 1.3

$$H_{\text{abs}}(\mathbf{u}) = - \left[\iint S(\mathbf{u}') P^*(\mathbf{u}') P(\mathbf{u}' + \mathbf{u}) d^2\mathbf{u}' + \iint S(\mathbf{u}') P^*(\mathbf{u}') P(\mathbf{u}' - \mathbf{u}) d^2\mathbf{u}' \right]$$

$$H_{\text{ph}}(\mathbf{u}) = i \left[\iint S(\mathbf{u}') P^*(\mathbf{u}') P(\mathbf{u}' + \mathbf{u}) d^2\mathbf{u}' - \iint S(\mathbf{u}') P^*(\mathbf{u}') P(\mathbf{u}' - \mathbf{u}) d^2\mathbf{u}' \right]$$

Equation 1.4

The weak object approximation is a linear approximation of the transmission function of a thin sample. The weak object approximation is commonly used when the phase delay corresponding to a sample is less than 0.65 radians. This allows the DPC forward model to be linearized into a sum of contributions from the background, absorption, and phase. In literature, the transfer functions for phase and absorption are referred to as weak optical transfer functions (WOTF's) and their closed form is shown in Equation 1.4, using the same notation as the previous equations. As seen in figure 1.5, the resulting absorption transfer function is a low-pass filter, while the resulting phase WOTF resembles an antisymmetric band-pass.

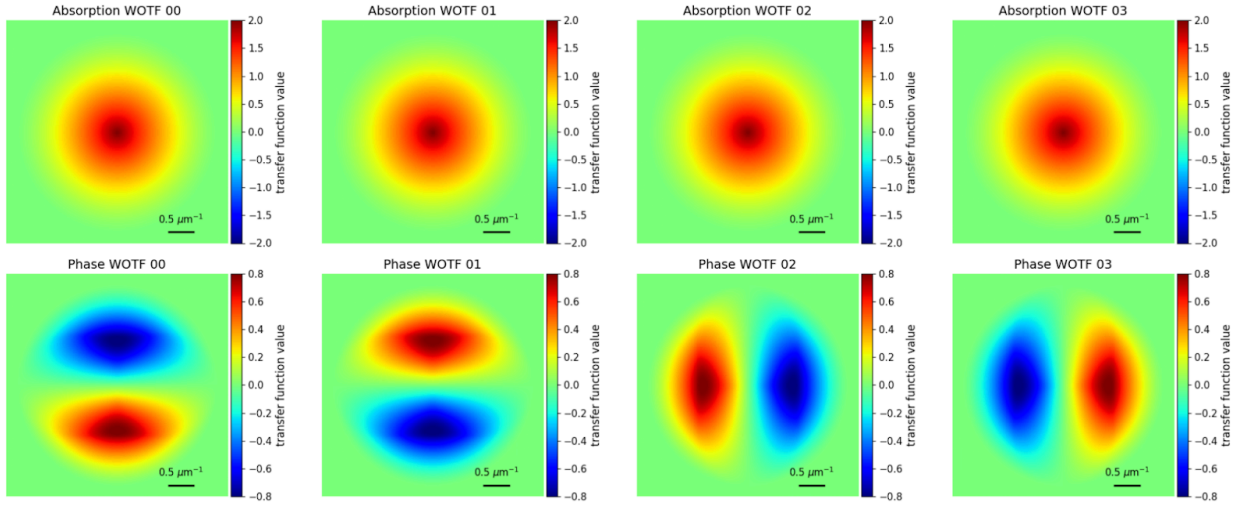


Figure 1.5: the Weak Optical Transfer Functions (WOTFs) corresponding to angled illumination from the bottom, top, left, and right half circles.

Using only the bright-field illuminations in a half-circular region containing angles up to the NA of the objective, DPC is able to achieve theoretical resolution up to twice the NA of the objective, thereby providing superior phase contrast as opposed to methods using coherent illumination such as TIE. A single half-circle illumination intensity image corresponds to a phase transfer function that contains zeros along the axis of asymmetry. By differencing opposite pairs of DPC illuminations, we are able to obtain qualitative phase images that contain frequencies along these missing directions, leading to high contrast images containing characteristic “shadows” where phase gradients are encountered.

The Differential Phase Contrast model approximates a derivative in phase. Phase retrieval from DPC thereby approximates integration along gradient boundaries. Due to noise introduced from measurements as well as mismatch between the real-world system and our forward model, which assumes a thin object, we introduce regularization in solving our inverse problem.

Tikhonov-regularization imposes a dampening factor that is applied equally across all spatial frequencies present in the measured data. In the Tikhonov-regularization case, the regularization term is a penalty on the squared loss of the recovered object's spectrum. This is done by solving the linear system in Equation 1.6. Tilde's denote the Fourier Transform Operation. I denotes DPC intensity measurements. H_j is a matrix whose blocks are matrices corresponding to the absorption and phase WOTF's. ϕ is a matrix consisting of the absorption and phase matrices concatenated $\phi = [\mu \ \varphi]^T$, and \cdot denoting element-wise multiplication. γ_{RE} and γ_{Im} are regularization coefficients, chosen based on the sample. Typically for a thin sample, a prior assumption is that the absorption terms are insignificant, so γ_{RE} is made large in order to account for this prior.

$$\min \sum_j \left\| \tilde{I}_{DPC,j}(u) - H_j(u) \cdot \tilde{\phi}(u) \right\|_2^2 + \gamma_{Re} \|\tilde{\phi}_{Re}\|_2^2 + \gamma_{Im} \|\tilde{\phi}_{Im}\|_2^2.$$

Equation 1.6

$$\begin{bmatrix} \tilde{\mu} \\ \tilde{\phi} \end{bmatrix} = \left(\begin{bmatrix} H_\mu & H_\phi \end{bmatrix}^* \begin{bmatrix} H_\mu \\ H_\phi \end{bmatrix} + \begin{bmatrix} \gamma_\mu & 0 \\ 0 & \gamma_\phi \end{bmatrix} \right)^{-1} \begin{bmatrix} H_\mu & H_\phi \end{bmatrix}^* \tilde{I}$$

Equation 1.7

The Tikhonov-regularization yields a closed form solution as shown in equation 1.7. * denotes conjugate, and $\gamma_{RE} = \gamma_\mu$, $\gamma_{Im} = \gamma_\phi$. This provides a simple and computationally cheap solution.

However, due to effects from high frequency noise and the discrepancy between the DPC forward model, which assumes a sum over infinitesimal point sources uniformly distributed on a half-circle, high-frequency noise is amplified in reconstructions where only Tikhonov regularization is used.

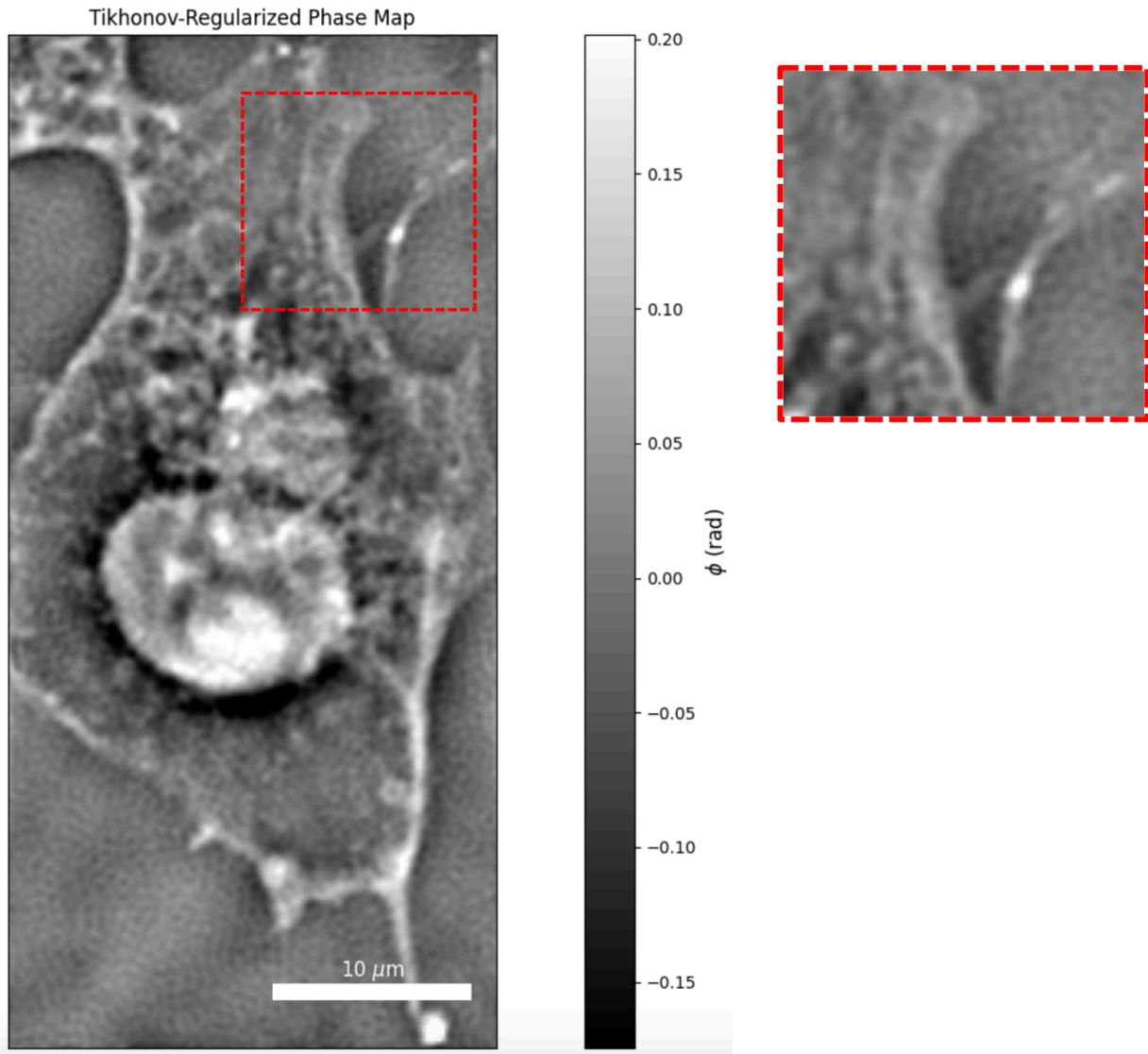


Figure 1.8: a QPI reconstruction from a single U2OS cell, with high frequency artifacts in the reconstruction from Tikhonov-Regularized deconvolution.

Another form of regularization is TV regularization, where a TV penalty term corresponding to a sparsity prior is used. Equation 1.9 shows the TV-regularized DPC objective function. The superscript d denotes the order of the difference operator. $d=1$ encourages sparsity in the first-differences, thereby yielding piecewise-flat solutions.

$$\min \sum_j \left\| \tilde{I}_{DPC,j}(u) - H_j(u) \cdot \tilde{\phi}(u) \right\|_2^2 + \gamma_{Re} \|\tilde{\phi}_{Re}\|_2^2 + \gamma_{Im} \|\tilde{\phi}_{Im}\|_2^2 + \tau \|\nabla^{(d)} \phi\|_1$$

Equation 1.9

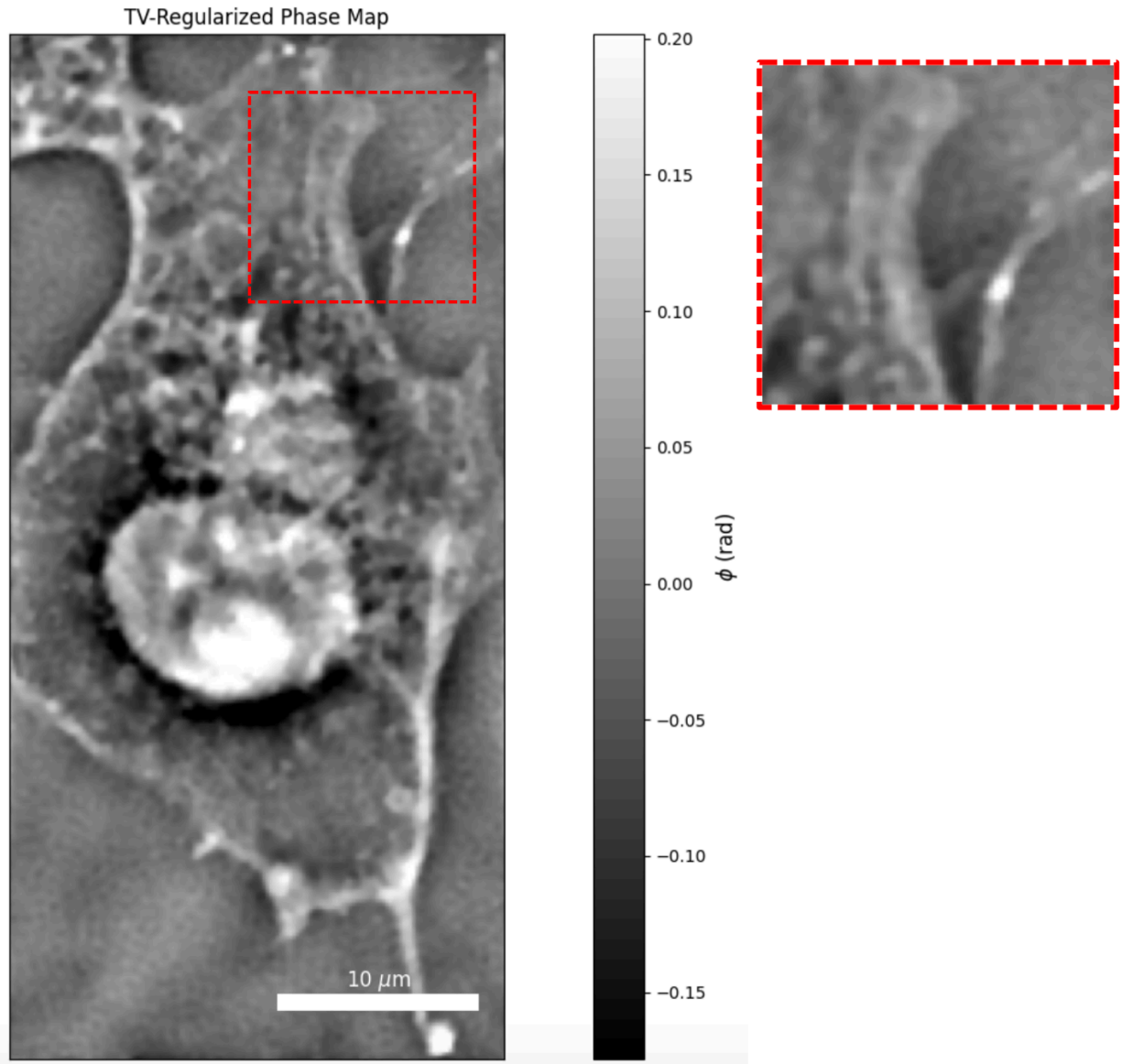


Figure 1.10: TV regularization reduces the high frequency intensity fluctuations in this cell image.

1c. Aberration Correction

In real-world applications, no microscopy system is completely free of aberrations. Optical aberrations limit the achievable resolution of microscopy systems. Furthermore, in phase-imaging techniques, aberrations introduce model mismatch between the real-world system and the forward model that is assumed in solving the relevant inverse problem. There are methods to estimate aberrations using wavefront sensors. Furthermore, there is an area of study

known as algorithmic self-calibration that aims to parametrize the aberrations and optimize an aberration function jointly with the reconstruction problem. Algorithmic self-calibration has been explored in Fourier Ptychography [18, 19] and extended to Differential Phase Contrast [10].

In the Differential Phase Contrast case, DPC measurements provide good phase contrast but very little aberration contrast, so aberration correction becomes an ill-posed problem given only DPC measurements. To provide aberration contrast, an additional coherent illumination measurement is used.

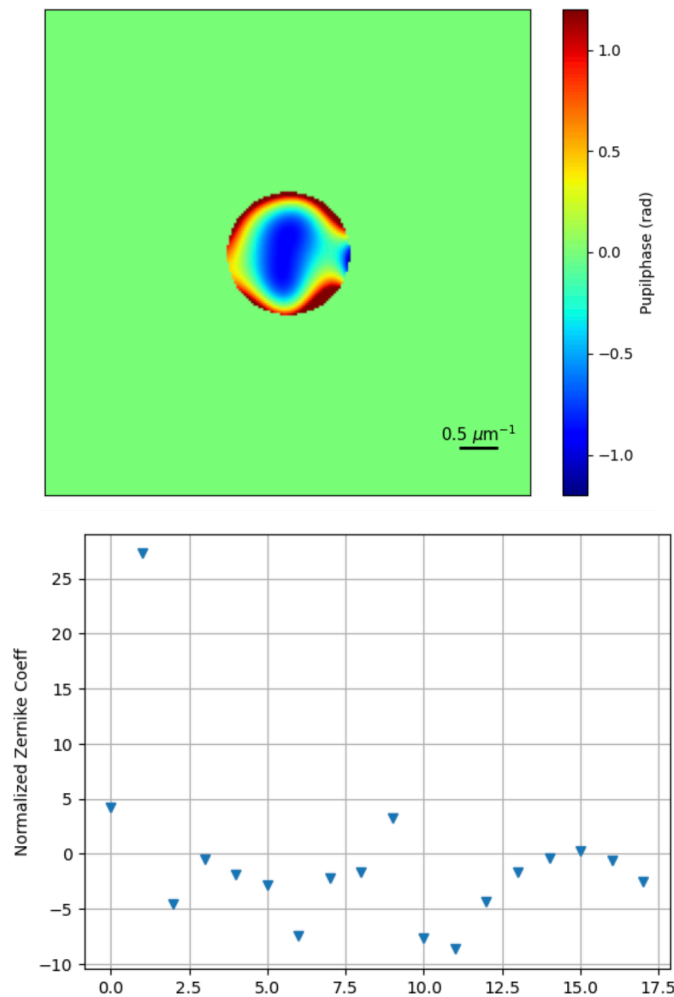


Fig 1.11: Above: example aberrated pupil phase. An aberration-free system would contain all 0's within the stop. Below: Zernike coefficients for the 3rd - 20th Zernike modes

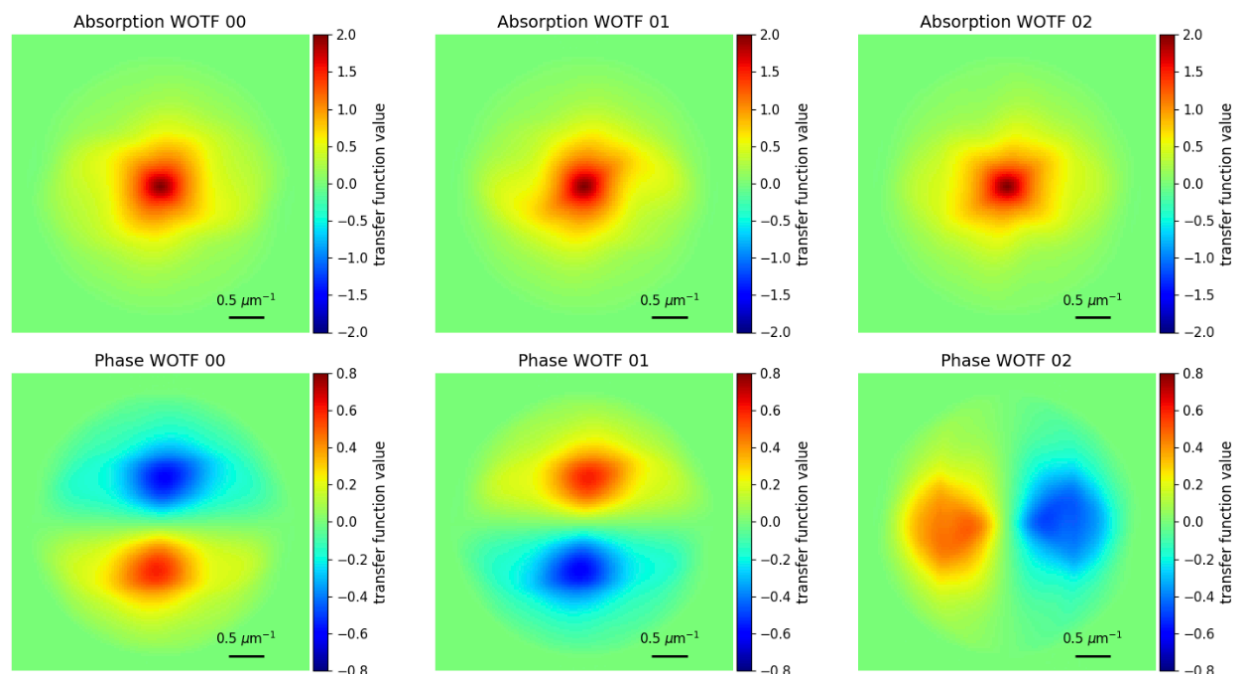


Fig 1.12: The WOTF's derived from the above pupil aberration. Note the loss of signal in the higher spatial frequencies compared to the unaberrated DPC case.

We use the DPC aberration correction procedure as discussed in [10]. This procedure parametrizes the aberration function as a phase term applied to the pupil.

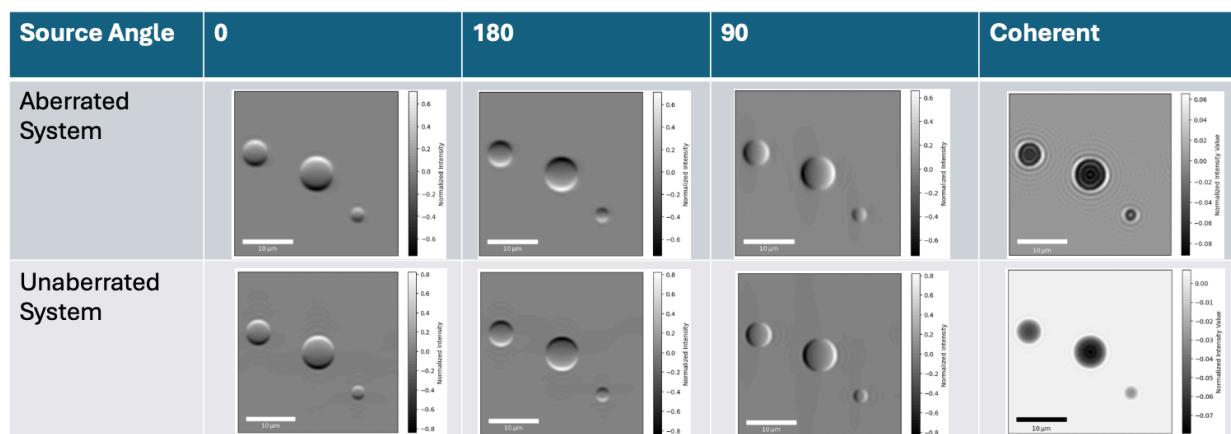


Fig 1.13: Simulated bead sample. DPC provides good phase contrast, but limited aberration contrast. Using coherent illumination, we see clear differences in the shape of the diffraction rings between the two cases

1d. Biological Applications

Quantitative Phase Imaging has applications in biology due to its ability to identify intracellular structures and soft tissues. This suggests applications in settings where traditionally invasive and time-consuming techniques have been used to perform such visualizations. One example of such an application is in Virtual Staining [3-5]. In traditional histological staining techniques,

chemicals such as Hematoxylin and eosin (H&E) are used to mark certain cell and tissue structures. While histological staining has been standard practice in the medical community, there are several drawbacks. Histological stains use toxic chemical compounds which alter the structure of biological samples. Furthermore, it is time-consuming and requires expertise to produce these stains, thereby making the procedure extremely costly. As an alternative to histological stains, virtual staining has been proposed, where a label-free methodology such as bright-field microscopy or a quantitative phase method is first used to produce an image of the sample. Then, a neural network is used to map the label-free image to a synthetic stained image, which is then used by a pathologist for various downstream applications. In order to train the image-translation models in virtual staining, a separate registration step is required, since the same sample must be stained after it was first imaged in a label-free manner. This introduces error due to the possibility of the sample being damaged during this procedure. Another method commonly used in virtual staining uses unsupervised learning and does not require a registration step. These methods typically utilize a generative model such as CycleGAN [21] or Pix2Pix [15] that is trained on large datasets of unpaired data, and the model learns to style transfer between the two groups. Empirically, unsupervised methods have been shown to underperform supervised methods when labeled data is available, and the computational cost is also costlier in the unsupervised case.

The work that is most similar to ours is the usage of label-free imaging to identify protein aggregates in neurons [11]. In this work, registered fluorescence and phase images are acquired, while a U-Net Convolutional Neural Network [14] is trained on labeled pairs. Previous work uses a coherent illumination technique where axial scans using coherent illumination at various defocus positions provide phase contrast. Compared to these methods, DPC provides better optical sectioning and up to two times better resolution due to the increase of effective NA due to partial coherence.

2. Multimodal Imaging Setup

In this section, we describe a microscopy system that we use to multiplex DPC and fluorescence measurements.

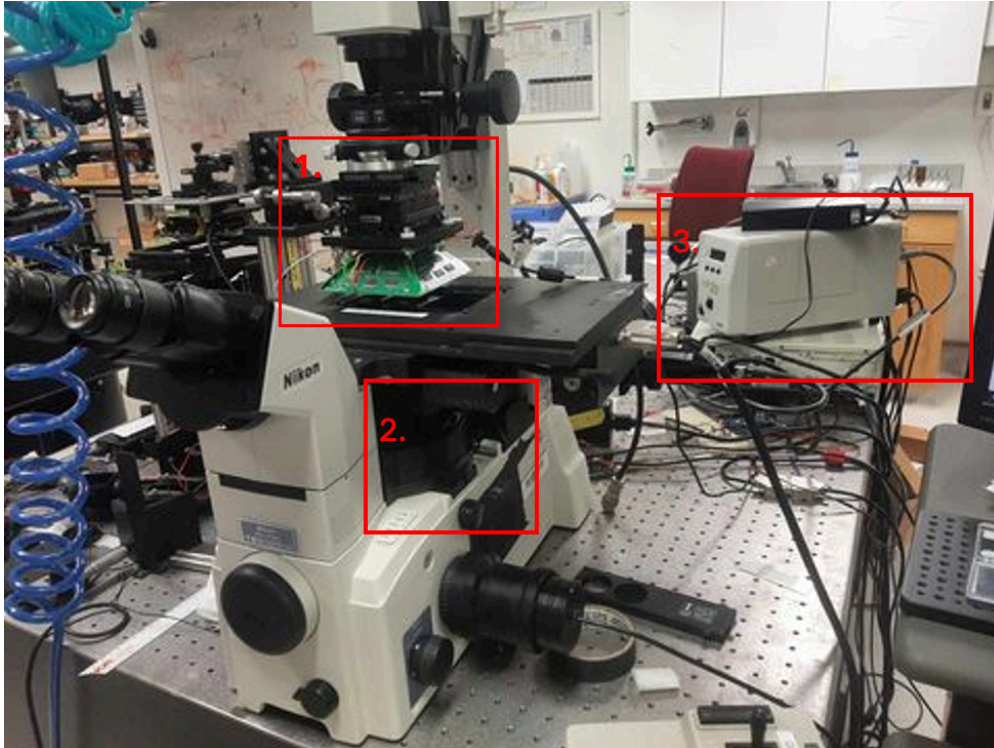


Figure 2.1: Our multimodal imaging septum which is built on a commercial inverted microscope. Box 1: the LED light source. Box 2: objective turret and filterwheel. Box 3: XCite 120PC Excitation source.

Our multimodal imaging setup consists of a commercial microscope (Nikon TE2000-U) with its illumination unit replaced by a programmable LED array. We use a broadband excitation light source for fluorescence channel measurements (XCite 120PC). A camera (CMOS Edge) is attached to the camera port on the microscope, allowing for capture of 2160x2560 full-FOV images. We utilize a 0.65/40x objective (nikon cfi plan), allowing for capture of high resolution differential phase contrast images. The resulting QPI techniques achieve phase images with effective NA of $0.65 * 2 = 1.3$ due to the use of partially coherent illumination from angles up to the bright-field cutoff. The diffraction-limited resolution formula yields $\frac{\lambda}{2*NA}$ for the spatial resolution limit. Thus, using red illumination with a wavelength of 625nm, we are able to attain a theoretical spatial resolution limit of 0.24 microns.

Lateral controls are made possible by the Proscan II stage, which can be controlled through user inputs to the appropriate port or though joystick controls. In this work, we also implemented axial controls by replacing the hand-turned focus knob with a focus motor, which can also be programmably controlled. We use custom Matlab scripts to alternate the source illumination and control the camera exposure time and trigger timing, as well as to control the shutter of the

excitation source. This enables us to automatically acquire registered DPC and fluorescence measurements.

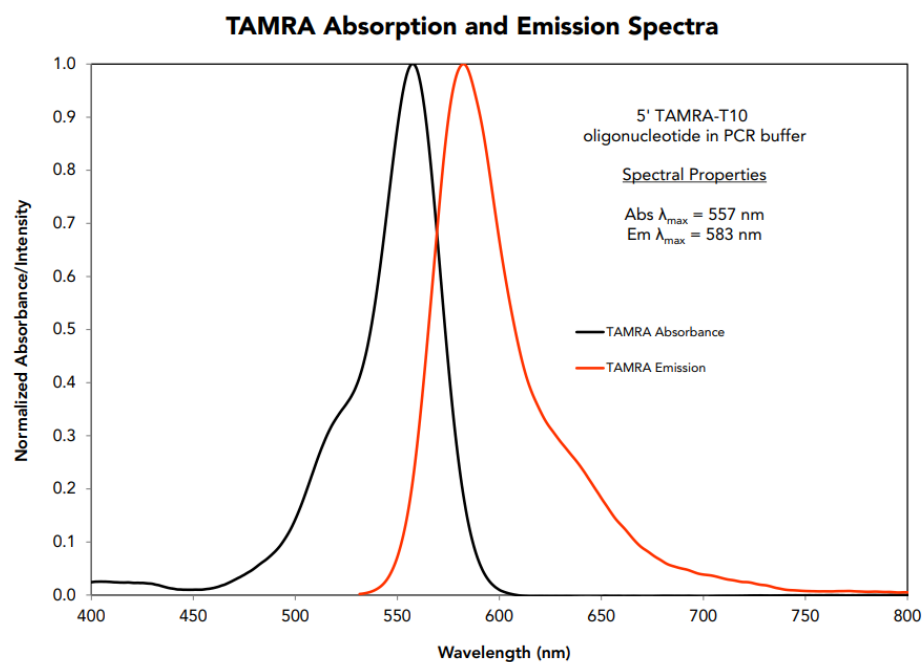


Figure 2.2: The excitation and absorption curves for the fluorescent compound fed to our U2OS samples. The red filtercube contains an excitation bandpass filter and an emittance bandpass filter, allowing us to capture both excitation and emission peaks.

3. U2OS Cell Dataset

Our collaborators provided us with a set of fixed cells from the U2OS (human osteosarcoma) line mounted on Petri dishes in PBS. The cells consist of a group which has been fed a toxic protein aggregate and a group of negative controls.

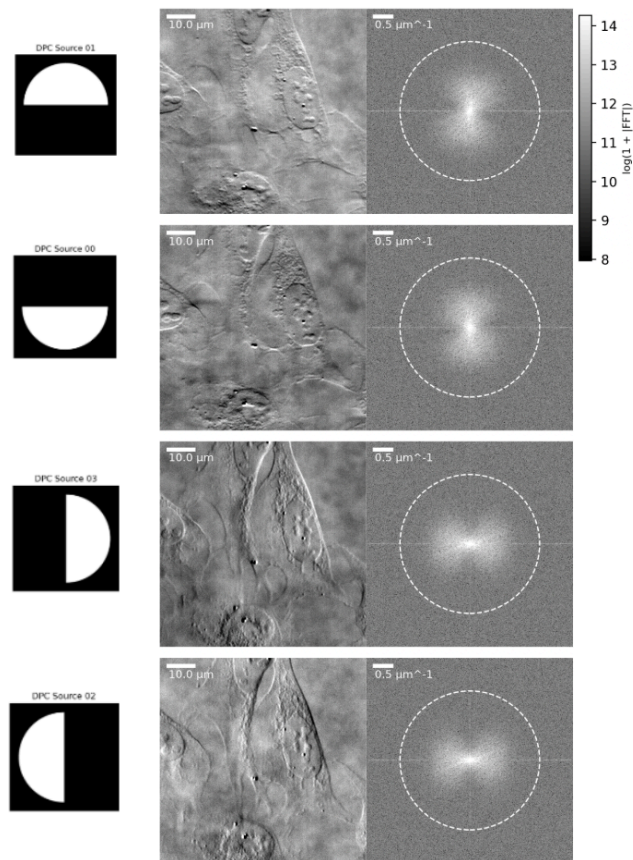


Figure 3.1: A subregion of the FOV which contains several U2OS cells. The left column shows the illumination source. The middle column contains the intensity measurement while the right column shows the spectrum, with the dashed circle representing the theoretical resolution cutoff of twice the NA of the objective. We note that the spectrum of each intensity image resembles the lobes present in the phase WOTF, which is expected because the cells are weakly absorbing.

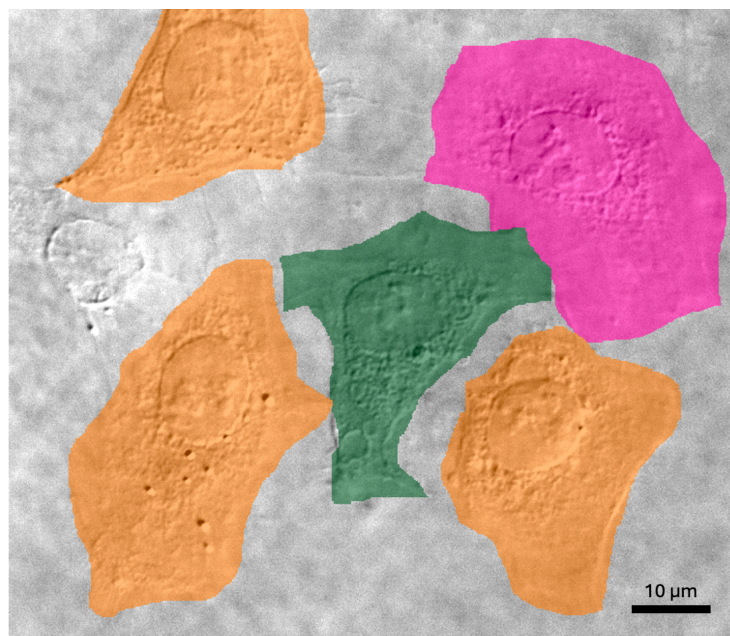


Figure 3.2: Annotations produced by fine-tuned Cellpose model

In order to isolate single-cell regions without contributions from background artifacts coming from defocused debris which is harmful for both quantitative phase reconstruction and downstream tasks, a segmentation step is necessary to isolate individual cells. Cellpose [12, 13] is a generalist architecture used for cell segmentation. Community contributions have led to foundation models that are pre-trained on thousands of manually annotated microscope images. We utilized a fine-tuned CellPose model to segment single-cell regions. The fine-tuning step is necessary because the base CellPose model (Cyto2) is only trained on Zernike qualitative phase images, and thus does not perform well on DPC images. We fine-tuned the segmentation model using DPC qualitative phase images for the best possible resolution. Qualitatively, this required only 40 manually labeled ROI's, each containing several distinct morphologies and labels for cells with distinct nuclei, for the CellPose model to learn how to draw high quality cell boundaries. Then using the bounds of each segmentation cell-mask, we are able to acquire rectangular single-cell regions containing little background contribution. Under the assumption of the DPC forward process being linear and spatially invariant, we are able to both save compute resources and eliminate the contributions from background intensity fluctuations in our reconstructions by running our QPI reconstruction algorithms on each bounding box separately. We manually removed cell images that contained insufficient phase contrast due to background debris and intensity fluctuations. After these steps, we produce a dataset consisting of 323 cells in the “positive” label class and 1538 negative controls.

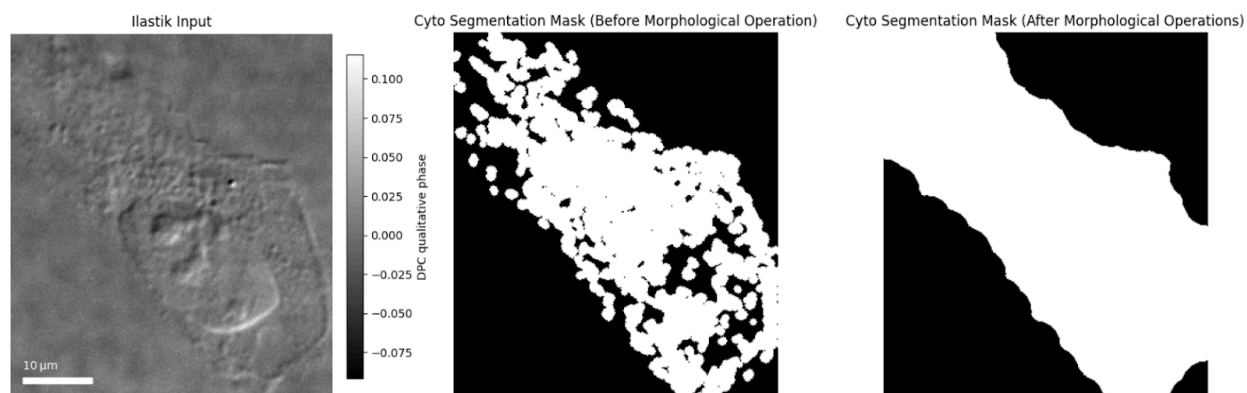
4. Statistical Analysis of DPC Measurements

In order to compare the differences in organelle morphology and density between the cells from our treatment group and those from our control group, we used an organelle segmentation model implemented using Ilastik[17], which is an opensource segmentation library providing a user interface for semantic segmentation of cell images using sparse user-annotated examples.

	σ_0	σ_1	σ_2	σ_3	σ_4	σ_5	σ_6	σ_7
Sigma	0.30	0.70	1.00	1.60	3.50	5.00	10.00	add
► Color/Intensity	<input type="checkbox"/>	<input type="checkbox"/>	<input type="checkbox"/>	<input type="checkbox"/>	<input type="checkbox"/>	<input type="checkbox"/>	<input type="checkbox"/>	<input type="checkbox"/>
▼ Edge		<input checked="" type="checkbox"/>						
Laplacian of Gaussian		<input checked="" type="checkbox"/>						
Gaussian Gradient Magnitude		<input checked="" type="checkbox"/>						
Difference of Gaussians		<input checked="" type="checkbox"/>						
▼ Texture		<input checked="" type="checkbox"/>						
Structure Tensor Eigenvalues		<input checked="" type="checkbox"/>						
Hessian of Gaussian Eigenvalue		<input checked="" type="checkbox"/>						

Figure 4.1: feature selections in Ilastik. Features are computed on DPC qualitative phase images. We omit the selection of Color/Intensity features to improve generalizability given fluctuations in LED lighting and SnR

The classification models implemented in Ilastik classify images on a per-pixel level. For best generalizability, we use a Random Forest Classifier using edge and texture-level features. Because this approach lacks spatial context apart from pixel-level features that include spatial context due to blurring operations, we also apply a separate morphological closing operation in order to produce contiguous segmentation boundaries of large label classes such as the cytosolic region and the background.



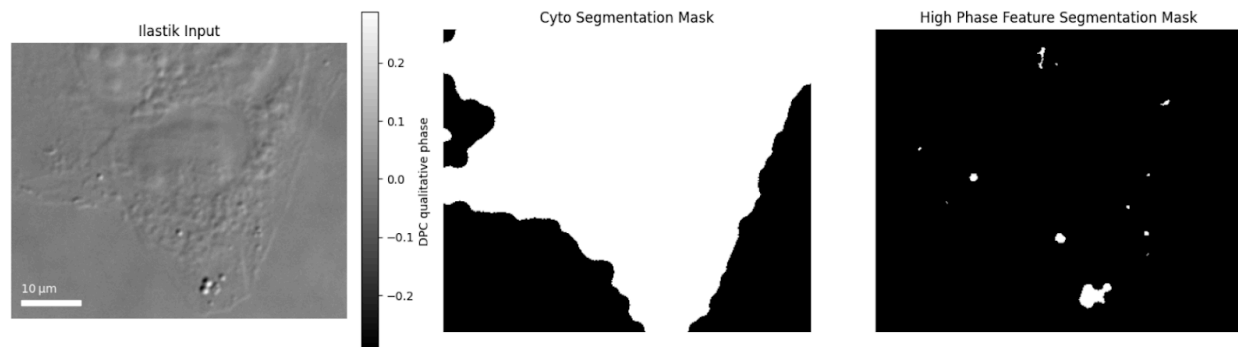
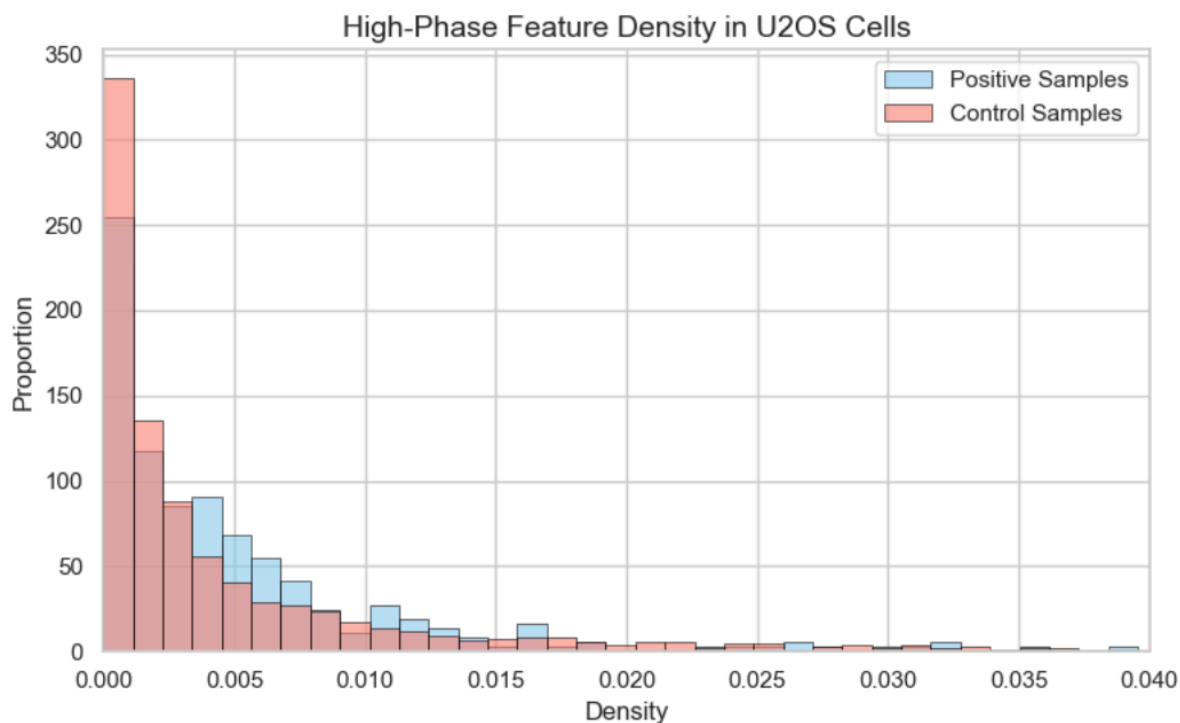


Figure 4.2: Segmentation Results. Above: post-processing steps on Ilastik output for Cyto segmentation. Below: High-phase-contrast feature segmentation.

One notable feature class was regions of high phase contrast (phase “bubbles”) that appear in the cytosolic regions of U2OS cells. We define the density of such features as the area of their segmentation mask over the area of the segmented region corresponding to the Cytosol. We compute this measure on cell images from the positive group to negative controls, observing that the distribution corresponding to diseased cells appears right-shifted with respect to the control cells. We use the Kolmogorov-Smirnov Test to test the statistical significance of the difference between the 2 distributions. The Kolmogorov-Smirnov Test yields a p-value of $9.53e-4$, suggesting the statistical significance of this difference.



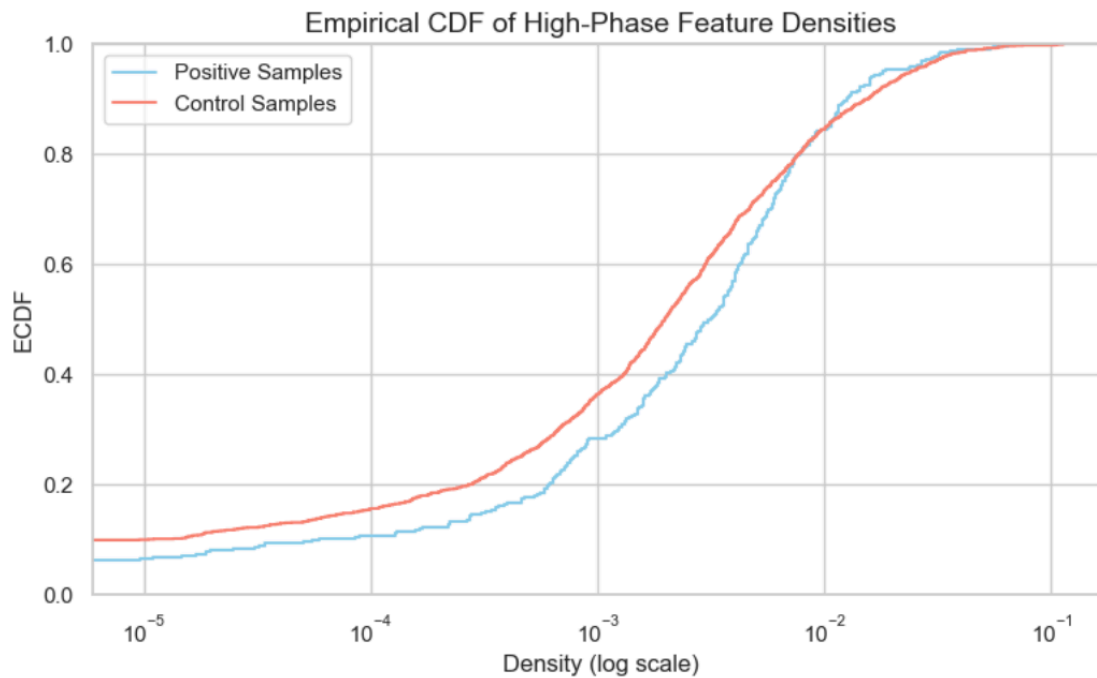


Figure 4.3: The distribution of high-phase features for Positive samples compared to the control set.

5. Methods in Deep-Learning

Image Classification

Due to the availability of samples in both control and treatment groups, we investigated the usage of convolutional neural networks to computationally classify cells.

We used a pytorch implementation of VGGNet [16], which is a convolutional neural network commonly used for image classification. We trained VGGNet models on both DPC qualitative phase (obtained by subtracting opposite pairs and dividing over their sum) and the corresponding QPI reconstructions. We trained our models on an NVIDIA RTX 5090 GPU, using the cross-entropy loss function and ADAM optimizer (betas=(0.9, 0.999)). We validated the performance of our classifier by using the ROC curve's Area-Under-Curve (AUC) on the testing set.

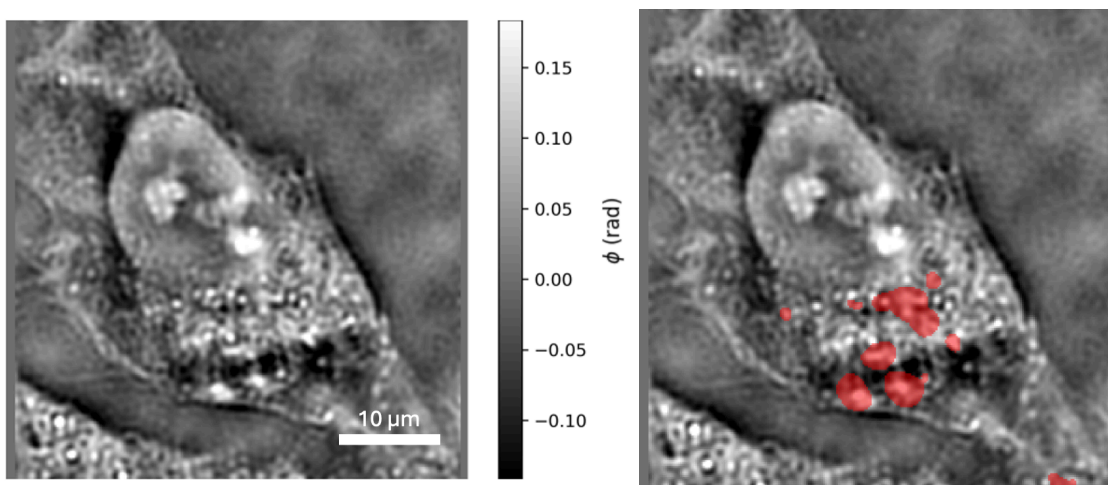


Figure 5.1: Left: An example quantitative phase reconstruction. Right: Overlay of QPI Reconstruction with thresholded fluorescence channel.

We compared the performance of the classification networks when trained on qualitative phase images versus QPI reconstructions obtained using Tikhonov regularization and a regularization coefficient of $1e-1$. This level of regularization was used due to the qualitative observation that it is able to eliminate background low-frequency content while preserving high spatial frequencies. Notably, the classifiers trained on our quantitative phase reconstructions did better than when trained on the qualitative phase data, suggesting that quantitative phase information encodes important information about the presence or lack thereof of protein aggregates and effectively removes problematic high and low-frequency noise through the use of regularization.

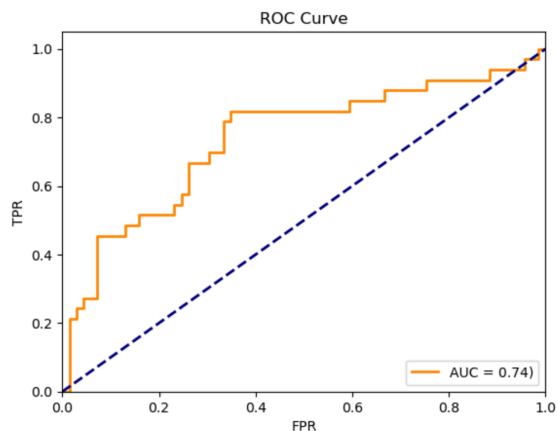
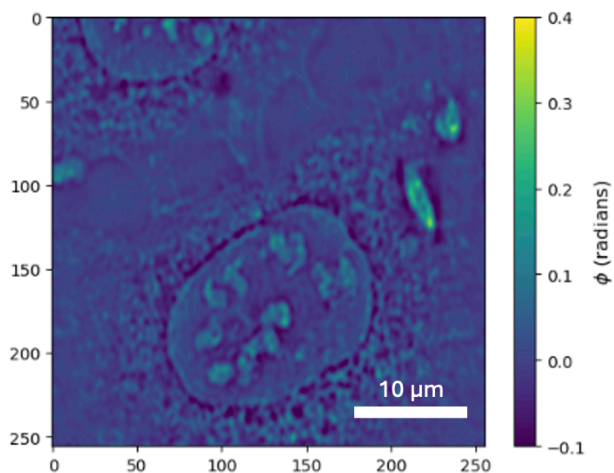


Figure 5.2: ROC curve for classifier performance on held-out set.

A classification network can also be used to do weakly supervised labeling of cell samples, which aims to make use of salient regions in the classification task in order to predict the location of protein aggregates in the labeled dataset. In order to do this, we implemented an attention mechanism on the baseline VGGNet as described in [22]. This creates a classifier that also enables interpretable attention maps that illustrate which regions are most salient for pixel classification. Qualitatively, it appears that the network attends to regions at different depths corresponding to their quantitative phase values. However, we do not observe high fluorescence intensity in all regions with high phase contrast, suggesting that additional investigation needs to be done in order to characterize the morphology of such structures.



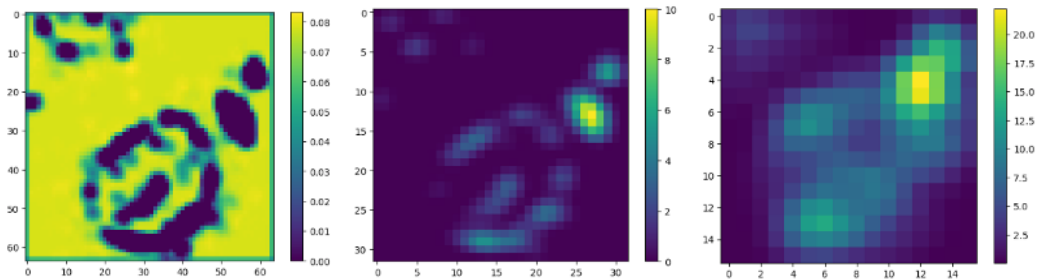


Figure 5.3: top: QPI input to Cell Classification. Bottom (left-to-right): Attention maps for earlier to later depths in the neural network.

6. Future Work

6a. Autofluorescence Filtering

An unexpected result from our initial datasets was the unwanted presence of autofluorescence in the red emission channel. Autofluorescence can come from unwanted debris such as dead cell parts or contamination from dust particles in the air. In contrast to TAMRA, autofluorescence contains a broadband emission spectrum, which suggests that the red channel's fluorescence measurements alone cannot isolate the signal coming from protein aggregates. In order to provide the most accurate quantitative information about the localization and density of protein aggregates, we include a set of filtercubes for green excitation wavelengths. Additional work must be done to assess the level of cross-talk between channels and to develop a postprocessing step for filtering out the autofluorescent structures.

6b. Extensions to 3D and Live-Cell Settings

The datasets that we captured in this work consist of fixed cells. In the future, our methods can be extended to study live-cell dynamics. However, several modifications are needed. In DPC microscopy, multiple images are needed for high quality reconstructions. For good coverage of the Fourier plane, it is necessary to take multiple images, which introduces the issue of motion registration. Neural space-time models (NSTM) [23] are a technique leveraging implicit neural representations to accurately register images along space and time. By using a NSTM, synthetic spatially-registered DPC datasets can be acquired and used for more accurate reconstruction of moving cells, and the original NSTM paper demonstrates successful performance of the method on DPC. NSTM learns spatially varying motion kernels that can be used to transform the DPC and fluorescence pairs, allowing for more accurate registration that can be done as a preprocessing step before the DPC reconstruction routine is invoked.

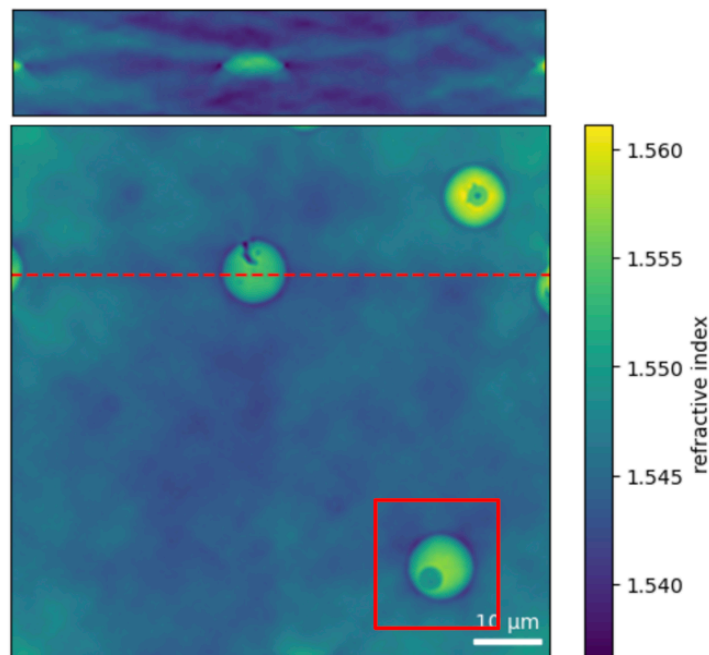


Fig 6.1: Above: x-z of labeled line. Below: x-y cross section of focus plane.

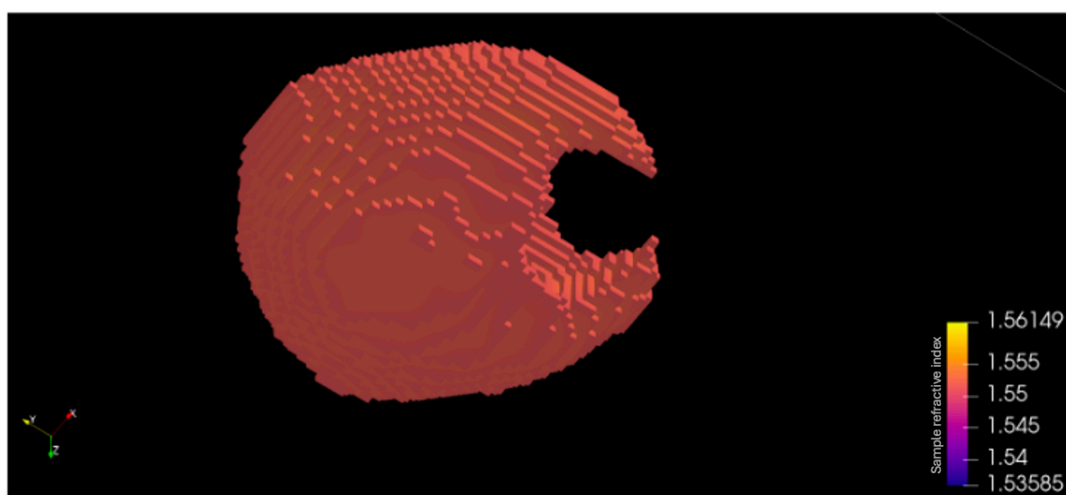


Figure 6.2: 3D reconstructions of the labeled borosilicate microsphere from the top figure. The microspheres have a mean diameter of 10 microns, and under the red wavelength have RI 1.56. The microspheres are immersed in closely index-matched oil (RI 1.544). Rendering produced using TomViz [24]

The analysis in this work extends only to QPI reconstructions in the 2D case due to our samples having limited depth, but we have additionally implemented an axial scanning mechanism using a motor attachment (Proscan Focus Drive) attached to the z focus-knob of the microscope. We have used this mechanism to construct accurate 3D refractive index reconstructions of test samples and performed high resolution reconstructions of samples using the open-source code provided alongside [8].

6c. Improvements to System Resolution

In Differential Phase Contrast, the theoretical maximum achievable resolution is determined by the NA of the objective and the wavelength. Thus, improvements can be made by using higher frequency illumination, or by using a more powerful objective lens. However, by using the typical half-circle pattern, there is a substantial drop-off in the SNR in the high spatial frequencies. In the original DPC work [7], a notable effect was that by using annular illumination patterns, there is better signal in these regions, allowing for better effective spatial resolution in the presence of noise.

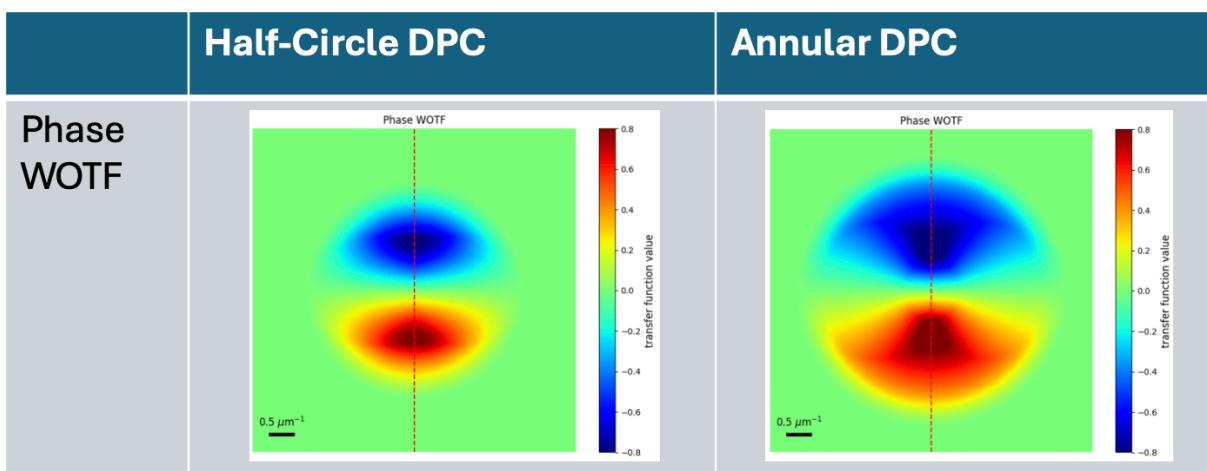


Figure 6.3: Side-by-side views of the Phase WOTF's corresponding to half-circle illumination with illumination angle up to the NA of the aperture (left) and illumination angles between 0.75 and 1.25 times the NA of the aperture (right). Notice that the WOTF for the annular illumination contains more substantial coverage of Fourier space from approximately the NA of the objective to twice the NA of the objective (diffraction-limited upper bound). WOTF's generated using the opensource Solver from [7].

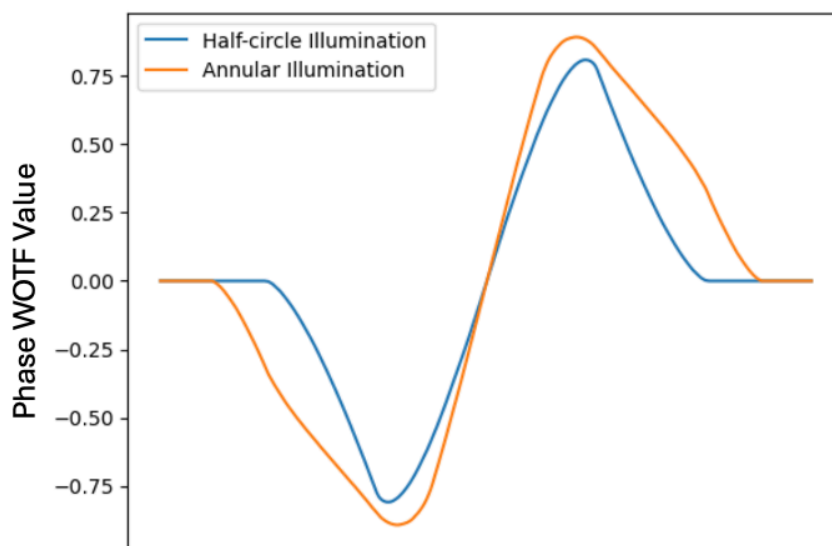


Figure 6.4: Annular illumination provides both improved signal for low and high spatial frequencies compared to the traditional half-circle patterns.

Bibliography

- [1] Z. F. Phillips, R. Eckert, and L. Waller, "Quasi-Dome: A Self-Calibrated High-NA LED Illuminator for Fourier Ptychography," in *Imaging and Applied Optics 2017 (3D, AIO, COSI, IS, MATH, pcAOP)*, OSA Technical Digest (online) (Optica Publishing Group, 2017), paper IW4E.5.
- [2] Bai, B., Yang, X., Li, Y. et al. Deep learning-enabled virtual histological staining of biological samples. *Light Sci Appl* 12, 57 (2023). <https://doi.org/10.1038/s41377-023-01104-7>
- [3] de Haan, K., Zhang, Y., Zuckerman, J.E. et al. Deep learning-based transformation of H&E stained tissues into special stains. *Nat Commun* 12, 4884 (2021). <https://doi.org/10.1038/s41467-021-25221-2>
- [4] Rivenson, Y., Liu, T., Wei, Z. et al. PhaseStain: the digital staining of label-free quantitative phase microscopy images using deep learning. *Light Sci Appl* 8, 23 (2019). <https://doi.org/10.1038/s41377-019-0129-y>
- [5] Zhang, Y., de Haan, K., Rivenson, Y. et al. Digital synthesis of histological stains using micro-structured and multiplexed virtual staining of label-free tissue. *Light Sci Appl* 9, 78 (2020). <https://doi.org/10.1038/s41377-020-0315-y>
- [6] Kataria, T., Knudsen, B., & Elhabian, S. Y. (2024). StainDiffuser: MultiTask Dual Diffusion Model for Virtual Staining (arXiv:2403.11340). arXiv. <https://arxiv.org/abs/2403.11340>
- [7] Lei Tian and Laura Waller, "Quantitative differential phase contrast imaging in an LED array microscope," *Opt. Express* 23, 11394-11403 (2015)
- [8] Chen M, Tian L, Waller L. 3D differential phase contrast microscopy. *Biomed Opt Express*. 2016 Sep 9;7(10):3940-3950. doi: 10.1364/BOE.7.003940. PMID: 27867705; PMCID: PMC5102530.
- [9] Zheng G, Horstmeyer R, Yang C. Wide-field, high-resolution Fourier ptychographic microscopy. *Nat Photonics*. 2013 Sep 1;7(9):739-745. doi: 10.1038/nphoton.2013.187. PMID: 25243016; PMCID: PMC4169052.
- [10] Michael Chen, Zachary F. Phillips, and Laura Waller, "Quantitative differential phase contrast (DPC) microscopy with computational aberration correction," *Opt. Express* 26, 32888-32899 (2018)

- [11] Ibrahim, K.A., Großmayer, K.S., Riguet, N. et al. Label-free identification of protein aggregates using deep learning. *Nat Commun* 14, 7816 (2023).
<https://doi.org/10.1038/s41467-023-43440-7>
- [12] Stringer, C., Wang, T., Michaelos, M., & Pachitariu, M. (2021). Cellpose: a generalist algorithm for cellular segmentation. *Nature methods*, 18(1), 100-106.
- [13] Pachitariu, M. & Stringer, C. (2022). Cellpose 2.0: how to train your own model. *Nature methods*, 1-8.
- [14] Ronneberger, O., Fischer, P., & Brox, T. (2015). U-Net: Convolutional Networks for Biomedical Image Segmentation. *arXiv*. <https://arxiv.org/abs/1505.04597>
- [15] Isola, P., Zhu, J.-Y., Zhou, T., & Efros, A. A. (2018). Image-to-image translation with conditional adversarial networks. *arXiv preprint arXiv:1611.07004*.
<https://arxiv.org/abs/1611.07004>
- [16] Simonyan, K., & Zisserman, A. (2015). Very Deep Convolutional Networks for Large-Scale Image Recognition. *arXiv preprint arXiv:1409.1556*. Retrieved from
<https://arxiv.org/abs/1409.1556>.
- [17] ilastik: interactive machine learning for (bio)image analysis
Stuart Berg, Dominik Kutra, Thorben Kroeger, Christoph N. Straehle, Bernhard X. Kausler, Carsten Haubold, Martin Schiegg, Janez Ales, Thorsten Beier, Markus Rudy, Kemal Eren, Jaime I Cervantes, Buote Xu, Fynn Beuttenmueller, Adrian Wolny, Chong Zhang, Ullrich Koethe, Fred A. Hamprecht & Anna Kreshuk
in: *Nature Methods*, (2019)
- [18] Roarke Horstmeyer, Xiaoze Ou, Jaebum Chung, Guoan Zheng, and Changhuei Yang, "Overlapped Fourier coding for optical aberration removal," *Opt. Express* 22, 24062-24080 (2014)
- [19] Xiaoze Ou, Guoan Zheng, and Changhuei Yang, "Embedded pupil function recovery for Fourier ptychographic microscopy," *Opt. Express* 22, 4960-4972 (2014)
- [20] N. Streibl, "Phase imaging by the transport equation of intensity," *Opt. Commun.* 49(1), 6–10 (1984).

- [21] Jun-Yan Zhu*, Taesung Park*, Phillip Isola, and Alexei A. Efros. "Unpaired Image-to-Image Translation using Cycle-Consistent Adversarial Networks", in IEEE International Conference on Computer Vision (ICCV), 2017.
- [22] Jetley, S., Lord, N. A., Lee, N., & Torr, P. H. S. (2018). Learn To Pay Attention. arXiv. <https://arxiv.org/abs/1804.02391>
- [23] Cao, Ruiming & Divekar, Nikita & Nuñez, James & Upadhyayula, Srigoikul & Waller, Laura. (2024). Neural space–time model for dynamic multi-shot imaging. *Nature Methods*. 21. 2336-2341. 10.1038/s41592-024-02417-0.
- [24] Real-time 3D analysis during electron tomography using tomviz, J. Schwartz et al., *Nature Comm.* 13, 4458 (2022).

Appendix

Code and Data Availability

Matlab scripts for the automated acquisition of DPC images, including with coherent illumination and 3D acquisition, along with our implementations/training loops for image classification neural networks, will be uploaded to the following repository:

https://github.com/william14641/EECS_MS_Project

Fluorescence intensities, Raw DPC measurements, as well as QPI reconstructions are available upon request.

Documents containing visualizations of the dataset, including DPC and fluorescence channels along with overlays, will be uploaded to the following Google Drive folder:

<https://drive.google.com/drive/folders/1DZp9cijKQQmKb-KFqaoI-KgEX91d4tu6?usp=sharing>